Frequency control by BESS for smooth Island transition of a hydro-powered microgrid

Citation for the original published paper (version of record):
Sunjaq, A., Chen, P., Bongiorno, M. et al (2024). Frequency control by BESS for smooth Island transition of a hydro-powered microgrid. IET Smart Grid, 7(1): 63-77.
http://dx.doi.org/10.1049/stg2.12140

Received: 11 May 2023 | Revised: 8 October 2023 | Accepted: 23 October 2023

IET Smart Grid

DOI: 10.1049/stg2.12140

ORIGINAL RESEARCH

Frequency control by BESS for smooth Island transition of a hydro-powered microgrid

Ahmed Sunjaq[1] | **Peiyuan Chen**[1] | **Massimo Bongiorno**[1] | **Ritwik Majumder**[1] | **Jan R. Svensson**[2]

[1]Department of Electrical Engineering, Chalmers University of Technology, Gothenburg, Sweden

[2]Hitachi Energy Research, Hitachi Energy, Västerås, Sweden

Correspondence

Ahmed Sunjaq.
Email: sunjaq@chalmers.se

Funding information

European Union's Horizon 2020 Research and Innovation Program, Grant/Award Numbers: 646039, 775970

Abstract

This paper develops a frequency control strategy for a battery energy storage system to facilitate the smooth island transition of a hydro-powered microgrid during unplanned grid outages. The proposed frequency control strategy uses a PI-based droop controller, where the tuning of the controller accounts for the limitations in the power response of a hydro generator and the required frequency quality of the microgrid. The effectiveness of the frequency control strategy is verified in Simulink using phasor simulations, and it is further validated in laboratory tests. The results demonstrate that the proposed PI-based droop and its tuning strategy fulfill the desired frequency quality requirement of the hydro-powered microgrid without over-dimensioning the size of the storage capacity as compared to the traditional proportional droop controller.

KEYWORDS

battery storage plants, distribution networks, frequency control, power system stability

1 | INTRODUCTION

Commercial and industrial (C&I) facilities are critical loads requiring a high degree of electricity supply reliability and resiliency [1–3], and the traditional N-1 supply reliability is not sufficient. Thus, many C&I facilities have their own local backup gas or diesel generators for island operation in case of grid outage. However, this generation type is not environmentally friendly, and many C&I facilities have set their own targets for reducing CO_2 emissions. One solution is to replace these fossil fuel powered generators with a battery energy storage system (BESS). However, long outage duration requires a large storage capacity, which makes the BESS uneconomical for C&I facility owners.

In Sweden, many C&I facilities are located close to a river where hydro generators are installed. For instance, a paper and pulp factory is supplied from the same substation to which a hydro-power plant (HPP) in a close-by river is connected [4]. Another example is the ongoing Ludvika microgrid project in Sweden, where hydro generators will power the local community in island operation if an outage occurs in the upstream grid [5]. However, the main reason that hydro generators do not take the main responsibility for frequency regulation in island operation is because of their technical limitations. These limitations include 1) limited fast frequency control capability caused by the regulation speed of the wicket gate and by the time delay of a long penstock [6–8] and 2) sustained frequency oscillations caused by the backlash in the gear when changing the direction of the wicket gate position [9]. One solution to assist the hydro generator for frequency regulation during island operation is to use a fast-acting device such as a BESS [10], which is interfaced to the grid by a voltage source inverter (VSI). Thus, how to design the frequency controller of the BESS in coordination with hydro generators for microgrid applications becomes a relevant issue.

Several existing studies available in the literature have addressed the frequency control of BESS in microgrid applications [11–17]. In microgrids with only inverter-based resources, the conventional proportional-based (P-based) droop controller is deployed for the frequency regulation of BESS in island operation [11–13]. However, for microgrids where both synchronous generators and inverter-based resources participate in frequency regulation, various droop-based frequency control strategies have been proposed for the BESS [14–17]. A P-based droop control with a non-linear droop constant is used in Ref. [14] for the BESS to improve the frequency regulation of a diesel-powered microgrid during island operation. A similar non-linear droop is proposed in Ref. [15] to improve the frequency stability of the Maui Hawaiian Island. The performance of the controller is good for small frequency deviations but deteriorates in case of large frequency disturbances as the droop constant increases. In Ref. [16], BESS and thermostatically controlled loads are used to provide fast frequency support in an islanded microgrid with a relatively slow diesel engine governor. The BESS frequency controller is modelled as a P-based droop, while the diesel engine is in isochronous control mode, which allows the BESS to contribute in frequency support dynamically without depleting the storage in a steady state. The authors in Ref. [17] propose a lag compensator for the frequency controller of BESS in a microgrid with a gas turbine. The strategy works well as the gas turbine has a fast frequency-regulating capability, which is not the case for hydro turbines. Consequently, such a frequency control strategy may not be able to fulfill the frequency nadir requirement in a hydro-powered microgrid. However, little literature has been found on the coordinated frequency control between BESS and hydro generators for microgrid applications.

On the other hand, for transmission system applications, there exists some literature on coordinated frequency control between BESS and hydro generators [18, 19]. A first-order high-pass filter-based frequency controller has been developed for coordinated frequency regulation between BESS and hydro generators [18]. However, the gain of the frequency controller is tuned to be similar to the transient gain of a hydro governor, which is typically very small and may not be sufficient for mitigating the frequency nadir in a low inertia system such as a microgrid. The authors in Ref. [19] propose a 4th order high-pass filter for the BESS to support hydro generators in grid frequency regulation. The filter parameters are tuned numerically for a specific system scenario, with no clear indication on how the control parameters should be adjusted when the system context changes such as for microgrid applications. Moreover, such a 4th order frequency control structure further complicates the parameter tuning in reality, where delays in programmable logic controllers and non-linearities in the turbine-governor system are present.

This paper aims to develop an energy-efficient frequency control strategy for a BESS to assist in the frequency regulation of a hydro-powered microgrid. The frequency controller is designed to handle the unplanned island transition of a microgrid, corresponding to one of the most severe power disturbances for this kind of the system. The main contributions of the paper are as follows:

1. It proposes the implementation of a lead compensator, which is equivalent to a PI-based droop control, in the frequency controller of the BESS. This compensator is designed to address the inherent delays in the hydro turbine-governor system.
2. The paper also presents a comprehensive tuning strategy for the lead compensator to achieve the online power distribution between the BESS and HPP. This strategy aims to achieve the desired steady-state power sharing and dynamic power coordination between the BESS and the hydro generator, all while minimising the consumption of energy storage resources. Additionally, the tuning strategy accounts for the permissible steady-state frequency deviation and frequency nadir of the microgrid during island operation.
3. The proposed BESS-HPP frequency coordination strategy utilises local frequency measurement signals and does not rely on communication. The coordination strategy is also verified in simulation and validated in the laboratory.

This paper is structured as follows. In Section 2, the microgrid network diagram is presented, and the mathematical model of the hydro turbine-governor system and BESS controller is summarised. Then, the proposed tuning of the BESS frequency controller is described in detail in Section 3, where the tuning strategy is summarised in Figure 5. In Section 4, the microgrid case study is first introduced, which is followed by the small-signal stability analysis of the proposed tuning. Section 5 presents the dynamic simulation results, where the proposed control strategy is compared with major existing strategies in the literature. Sensitivity analyses of the controller parameters on the performance of the frequency controller during microgrid island transition is also conducted. The proposed strategy is further validated through a laboratory experiment in Section 6. Section 7 discusses key assumptions made in the modelling and their implications. Finally, key findings are summarised in Section 8.

2 | MICROGRID MODEL FOR ISLAND TRANSITION STUDIES

2.1 | Network diagram of microgrid

Figure 1 shows the network diagram of an actual medium-voltage distribution system in the west coast of Sweden to be operated as a microgrid. The paper and pulp factory is supplied from a 140/11 kV substation to which a HPP is also connected. To enable a smooth island transition of the microgrid, a BESS is installed at the factory bus. In the following sections, we elaborate on the control adopted for each of the hydro and BESS systems.

2.2 | Hydro turbine with governor and exciter model

Figure 2 shows a generic Francis hydro turbine model for the provision of frequency containment reserve (FCR). The model includes a speed governor, an actuator of the wicket gate with a ramp rate limiter and a turbine and penstock model [20]. The automatic voltage controller (AVR) of the hydro generator is implemented as a standard PI controller with a static exciter

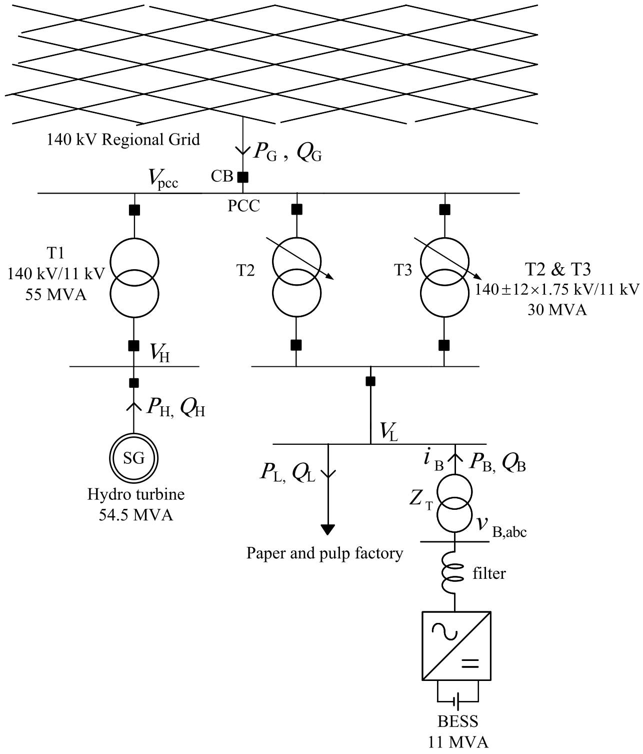

FIGURE 1 Hydro-powered microgrid equipped with a BESS to facilitate a smooth island transition of a paper and pulp facility.

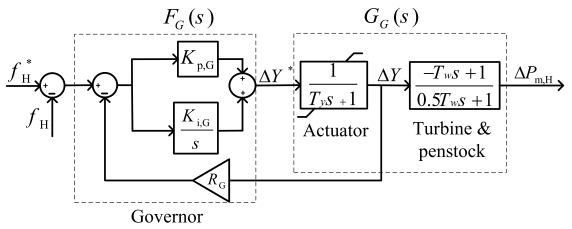

FIGURE 2 Simplified model of a Francis hydro turbine and governor for the provision of frequency containment reserve.

model typically used in the Nordic 32 power system model [21]. For a detailed description of the AVR and the exciter model, the readers are referred to Ref. [21].

The open-loop transfer function of the output mechanical power with respect to the input frequency deviation of the hydro turbine can be expressed as

$$\frac{\Delta P_{\mathrm{m,H}}}{-\Delta f_{\mathrm{H}}} = \left(\Gamma_{\mathrm{tr,G}}\frac{T_{\mathrm{G}}s}{T_{\mathrm{G}}s+1} + \Gamma_{\mathrm{ss,G}}\frac{1}{T_{\mathrm{G}}s+1}\right)\left(\frac{S_{\mathrm{b}}^{\mathrm{MG}}}{P_{\mathrm{b}}^{\mathrm{H}}}\right) \left(\frac{1}{T_{\mathrm{y}}s+1}\right)\left(\frac{-T_{\mathrm{w}}s+1}{0.5T_{\mathrm{w}}s+1}\right), \tag{1}$$

where $\Delta f_{\mathrm{H}} = f_{\mathrm{H}} - f_{\mathrm{H}}^{*}$, and

$$\Gamma_{\mathrm{ss,G}} = \frac{1}{R_{\mathrm{G}}}\frac{P_{\mathrm{b}}^{\mathrm{H}}}{S_{\mathrm{b}}^{\mathrm{MG}}}, \tag{2a}$$

$$\Gamma_{\mathrm{tr,G}} = \frac{K_{\mathrm{p,G}}}{1+R_{\mathrm{G}}K_{\mathrm{p,G}}}\frac{P_{\mathrm{b}}^{\mathrm{H}}}{S_{\mathrm{b}}^{\mathrm{MG}}}, \tag{2b}$$

$$T_{\mathrm{G}} = \frac{1+R_{\mathrm{G}}K_{\mathrm{p,G}}}{R_{\mathrm{G}}K_{\mathrm{i,G}}}. \tag{2c}$$

In the previous equations, $\Gamma_{\mathrm{ss,G}}$ is the governor steady-state frequency regulation strength, $\Gamma_{\mathrm{tr,G}}$ is the governor transient frequency regulation strength, T_{G} is the governor time constant, $P_{\mathrm{b}}^{\mathrm{H}}$ is the HPP rated active power, and $S_{\mathrm{b}}^{\mathrm{MG}}$ is the microgrid base power. Note that the conventional PI-based droop of the hydro governor with the parameters, $K_{\mathrm{p,G}}$, $K_{\mathrm{i,G}}$ and R_{G}, is equivalent to a high-pass filter plus low-pass filter with the parameters, $\Gamma_{\mathrm{ss,G}}$, $\Gamma_{\mathrm{tr,G}}$ and T_{G}. In this paper, the former parameters are expressed in per unit with respect to the HPP rated active power $P_{\mathrm{b}}^{\mathrm{H}}$, while the latter parameters are expressed in per unit with respect to the microgrid base power $S_{\mathrm{b}}^{\mathrm{MG}}$.

2.3 | Control of BESS

2.3.1 | Grid-following versus grid-forming control

Traditionally, BESS is controlled in a grid-following (GFL) mode when connected to a strong grid. However, the GFL control has shown poor small-disturbance stability under weak grid connection when using phase-locked-loop (PLL) for grid synchronisation [22]. In contrast, the grid-forming (GFM) control typically uses active power relation for obtaining the synchronisation angle and has shown a better stability performance under a weak grid or island operation [23]. Furthermore, the use of GFM control makes it easier for the BESS to transition between the grid-connected and island operation modes without switching the controller for obtaining the synchronisation angle, especially during an unplanned islanding event. This also mitigates the impact of island detection delay [23, 24]. Thus, the GFM control will be implemented in this paper.

2.3.2 | Implemented grid-forming control structure

Figure 3 shows a standard GFM control structure of a BESS for both grid-connected and island operation in a microgrid [25]. The active power controller calculates the synchronisation angle of the inverter [26]. The PI-based active power controller in Ref. [27] is adopted in this work. The voltage controller uses an integrator-based droop control. A virtual impedance is implemented to calculate the reference current, which is sent to the vector current controller for calculating the reference voltage that the converter should output. The proposed frequency controller will be discussed in the following subsections.

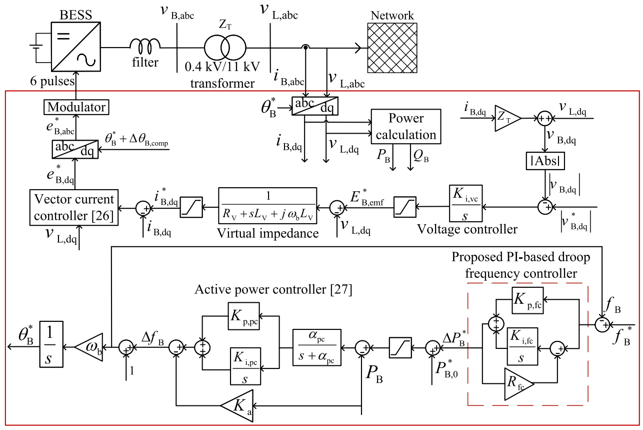

FIGURE 3 Implemented grid forming control of BESS.

2.3.3 | Proposed PI-based droop for frequency control of BESS

This work proposes a PI-based droop for a frequency controller in cascade with an active power controller. Figure 3 shows the corresponding control diagram. The open-loop transfer function of the frequency controller can be expressed as

$$\frac{\Delta P^*_B}{-\Delta f_B} = \left(\Gamma_{\mathrm{tr,fc}} \frac{T_{\mathrm{fc}} s}{T_{\mathrm{fc}} s + 1} + \Gamma_{\mathrm{ss,fc}} \frac{1}{T_{\mathrm{fc}} s + 1}\right)\left(\frac{S_b^{\mathrm{MG}}}{P_b^{\mathrm{B}}}\right), \tag{3}$$

where $\Delta f_B = f_B - f^*_B$, and

$$\Gamma_{\mathrm{ss,fc}} = \frac{1}{R_{\mathrm{fc}}} \frac{P_b^{\mathrm{B}}}{S_b^{\mathrm{MG}}}, \tag{4a}$$

$$\Gamma_{\mathrm{tr,fc}} = K_{\mathrm{p,fc}} \frac{P_b^{\mathrm{B}}}{S_b^{\mathrm{MG}}}, \tag{4b}$$

$$T_{\mathrm{fc}} = \frac{1}{R_{\mathrm{fc}} K_{\mathrm{i,fc}}}. \tag{4c}$$

In the previous equations, $\Gamma_{\mathrm{ss,fc}}$ is the steady-state frequency regulation strength of the BESS frequency controller, $\Gamma_{\mathrm{tr,fc}}$ is the transient regulation strength, T_{fc} is the frequency controller time constant, and P_b^{B} is the BESS rated active power. Note that the PI-based droop of the BESS frequency controller with the parameters, $K_{\mathrm{p,fc}}$, $K_{\mathrm{i,fc}}$ and R_{fc}, is equivalent to a high-pass filter plus low-pass filter with the parameters, $\Gamma_{\mathrm{ss,fc}}$, $\Gamma_{\mathrm{tr,fc}}$ and T_{fc}. In this paper, the former parameters are expressed in per unit with respect to the BESS rated active power P_b^{B}, while the latter parameters are expressed in per unit with respect to the microgrid base power S_b^{MG}.

2.4 | Microgrid island detection

A communication-based island detection is used by monitoring the breaker status of the grid in-feed line. The communication is usually based on Ethernet cable or optical fibre, and the communication delay is in the order of a few milliseconds and has little impact on the controller response [28]. A passive island detection method, for example, based on local frequency measurement, is typically adopted to handle communication failure [29]. The impact of communication failure will be discussed later.

3 | PROPOSED TUNING OF BESS FREQUENCY CONTROLLER

In the case that only the BESS regulates the microgrid frequency during island transition, the classical P-based droop control can be adopted as described inRefs. [11–13]. This will not be further discussed. This paper focuses on cases where the BESS is used to assist HPP in regulating the microgrid frequency during island transition.

3.1 | Criteria for smooth island transition

The following two criteria are specified for the microgrid to achieve a smooth island transition:

- maximum instantaneous frequency deviation ($\Delta f^{\max}$).
- maximum steady-state frequency deviation $\left(\Delta f_{\mathrm{ss}}^{\max}\right)$.

Steady-state here refers to the period of time after the frequency has stabilised and before the activation of the secondary frequency reserve to restore the frequency to 50 Hz.

3.2 | Steady-state power sharing between BESS and HPP

To fulfill the requirement on the maximum allowed steady-state frequency deviation $\Delta f_{\mathrm{ss}}^{\max}$, the minimum required frequency regulation strength of the microgrid $\Gamma_{\mathrm{ss,tot}}^{\min}$ should be set according to

$$\Gamma_{\mathrm{ss,tot}}^{\min} = -\frac{\Delta P_{\mathrm{dm}}}{\Delta f_{\mathrm{ss}}^{\max}} - D_L, \tag{5}$$

where ΔP_{dm} is the dimensioning disturbance and D_L is the load frequency dependence. Both ΔP_{dm} and D_L are in per unit with respect to microgrid base power S_b^{MG}. If the frequency regulation strength of the hydro turbine $\Gamma_{\mathrm{ss,G}} \geq \Gamma_{\mathrm{ss,tot}}^{\min}$, there is no need for the BESS to provide a steady-state frequency reserve, that is, $\Gamma_{\mathrm{ss,fc}} = 0$. However, if $\Gamma_{\mathrm{ss,G}} < \Gamma_{\mathrm{ss,tot}}^{\min}$, then the BESS needs to provide the missing frequency reserve in a steady state. In summary, the BESS regulation strength $\Gamma_{\mathrm{ss,fc}}$ is

$$\Gamma_{\mathrm{ss,fc}} = \begin{cases} 0, & \Gamma_{\mathrm{ss,G}} \geq \Gamma_{\mathrm{ss,tot}}^{\min} \\ \dfrac{-\Delta P_{\mathrm{dm}}}{\Delta f_{\mathrm{ss}}^{\max}} - D_L - \dfrac{1}{R_G} \dfrac{P_b^{\mathrm{H}}}{S_b^{\mathrm{MG}}}. & \Gamma_{\mathrm{ss,G}} < \Gamma_{\mathrm{ss,tot}}^{\min} \end{cases} \tag{6}$$

In the case of $\Gamma_{\mathrm{ss,fc}} = 0$, the frequency controller reduces to a high-pass filter with a transient gain of $\Gamma_{\mathrm{tr,fc}}$ (HF-based) according to Equation (3).

3.3 | Proposed dynamic power coordination between the BESS and HPP

As the hydro turbine-governor system has limited power ramping capability, the BESS is deployed to provide a fast power response to fulfill the maximum allowed instantaneous frequency deviation during an unintentional islanding event of the microgrid.

3.3.1 | Design of transient regulation strength of BESS

To fulfill the maximum allowed instantaneous frequency deviation ($\Delta f^{\max}$), the total transient regulation strength of the microgrid should be set at least according to

$$\Gamma_{\mathrm{tr,tot}}^{\min} = -\frac{\Delta P_{\mathrm{dm}} + D_{\mathrm{L}}\Delta f^{\max}}{\Delta f^{\max}}. \tag{7}$$

The total transient regulation strength of the microgrid corresponds to that of the HPP and BESS. Figure 4 shows the bode diagram of the hydro-turbine-governor system (solid blue curve) and BESS (solid green curve) according to (1) and (3), respectively. It is clearly seen that the hydro gain decays rapidly for frequencies above 10 rad/s. Therefore, the contribution of hydro to transient regulation strength is neglected. Thus, the transient regulation strength of the BESS frequency controller is designed as

$$\Gamma_{\mathrm{tr,fc}} = \begin{cases} \Gamma_{\mathrm{tr,tot}}^{\min}, & \Gamma_{\mathrm{ss,fc}} < \Gamma_{\mathrm{tr,tot}}^{\min} \\ \Gamma_{\mathrm{ss,fc}}. & \Gamma_{\mathrm{ss,fc}} \geq \Gamma_{\mathrm{tr,tot}}^{\min} \end{cases} \tag{8}$$

In the case of $\Gamma_{\mathrm{ss,fc}} \geq \Gamma_{\mathrm{tr,tot}}^{\min}$, the frequency controller transient gain is designed to be equal to its steady-state gain, that is, $\Gamma_{\mathrm{tr,fc}} = \Gamma_{\mathrm{ss,fc}}$. Thus, the PI-based droop controller reduces to a P-based droop controller according to Equation (3).

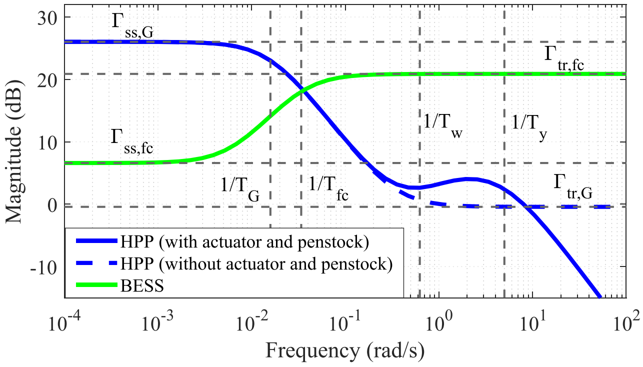

FIGURE 4 Bode magnitude plot of HPP and BESS according to the transfer functions given by Equations (1) and (3), respectively.

3.3.2 | Design of frequency controller time constant (T_{fc})

The BESS frequency controller time constant T_{fc} determines, relatively, how long will the BESS support the microgrid with the transient regulation strength. Thus, the time constant tuning also has a critical role in achieving a smooth island transition. The tuning of the BESS frequency controller time constant is also divided into two cases, depending on whether the HPP has sufficient reserve to cover the largest power imbalance.

BESS and HPP share steady-state reserves

Two sub-cases are considered under this case, depending on the frequency controller structure of the BESS whether it is a P-based droop or a PI-based droop. The controller structure can be found by looking at the relation between $\Gamma_{\mathrm{tr,fc}}$ and $\Gamma_{\mathrm{ss,fc}}$ of the BESS frequency controller. According to Equations (6) and (8) for the BESS frequency controller, it is not difficult to find that

$$\begin{cases} \Gamma_{\mathrm{tr,fc}} = \Gamma_{\mathrm{ss,fc}}, & \dfrac{1}{R_{\mathrm{G}}} \leq |\Delta P_{\mathrm{dm}}| \left(\dfrac{1}{|\Delta f_{\mathrm{ss}}^{\max}|} - \dfrac{1}{|\Delta f^{\max}|} \right) \dfrac{S_{\mathrm{b}}^{\mathrm{MG}}}{P_{\mathrm{b}}^{\mathrm{H}}} \\ \Gamma_{\mathrm{tr,fc}} > \Gamma_{\mathrm{ss,fc}}. & |\Delta P_{\mathrm{dm}}| \left(\dfrac{1}{|\Delta f_{\mathrm{ss}}^{\max}|} - \dfrac{1}{|\Delta f^{\max}|} \right) \dfrac{S_{\mathrm{b}}^{\mathrm{MG}}}{P_{\mathrm{b}}^{\mathrm{H}}} < \dfrac{1}{R_{\mathrm{G}}} \\ & < \left(\left| \dfrac{\Delta P_{\mathrm{dm}}}{\Delta f_{\mathrm{ss}}^{\max}} \right| - D_{\mathrm{L}} \right) \dfrac{S_{\mathrm{b}}^{\mathrm{MG}}}{P_{\mathrm{b}}^{\mathrm{H}}} \end{cases}$$

The design of the BESS frequency controller time constant corresponding to these two cases will be illustrated in the following sections.

(i) $\frac{1}{R_{\mathrm{G}}} \leq |\Delta P_{\mathrm{dm}}| \left(\frac{1}{|\Delta f_{\mathrm{ss}}^{\max}|} - \frac{1}{|\Delta f^{\max}|} \right) \frac{S_{\mathrm{b}}^{\mathrm{MG}}}{P_{\mathrm{b}}^{\mathrm{H}}}$

This case arises when the HPP has a very large droop constant R_{G} and thus provides a very small amount of reserve in a steady state, whereas BESS needs to provide a rather high amount of reserve in a steady state. As in this case, $\Gamma_{\mathrm{tr,fc}} = \Gamma_{\mathrm{ss,fc}}$, the controller reduces to a P-based droop, and the time constant T_{fc} becomes irrelevant.

(ii) $|\Delta P_{\mathrm{dm}}| \left(\frac{1}{|\Delta f_{\mathrm{ss}}^{\max}|} - \frac{1}{|\Delta f^{\max}|} \right) \frac{S_{\mathrm{b}}^{\mathrm{MG}}}{P_{\mathrm{b}}^{\mathrm{H}}} < \frac{1}{R_{\mathrm{G}}} < \left(\left| \frac{\Delta P_{\mathrm{dm}}}{\Delta f_{\mathrm{ss}}^{\max}} \right| - D_{\mathrm{L}} \right) \frac{S_{\mathrm{b}}^{\mathrm{MG}}}{P_{\mathrm{b}}^{\mathrm{H}}}$

This case arises when the HPP has a relatively small droop that provides a high amount of reserve in a steady state, whereas the BESS provides a relatively small amount of reserve in a steady state. In this case, the BESS has a higher regulation strength during transients than in a steady state, and tuning the time constant T_{fc} is crucial for meeting the frequency quality requirements. The criteria used for tuning the time constant T_{fc} is that the total power from the HPP and BESS should be monotonically increasing when applying a step change in the reference frequency, that is,

$$\frac{d}{dt}\Delta P_{\mathrm{tot}}(t) \geq 0, \tag{9}$$

where $\Delta P_{\mathrm{tot}}(t) = \Delta P_{\mathrm{m,H}}(t)\frac{P_{\mathrm{b}}^{\mathrm{H}}}{S_{\mathrm{b}}^{\mathrm{MG}}} + \Delta P_{\mathrm{B}}^{*}(t)\frac{P_{\mathrm{b}}^{\mathrm{B}}}{S_{\mathrm{b}}^{\mathrm{MG}}}$. $\Delta P_{\mathrm{m,H}}(t)$ and $\Delta P_{\mathrm{B}}^{*}(t)$ are defined as the unit step responses of the hydro governor (according to (1)) and BESS frequency controller (according to (3)), respectively. It is not difficult to find out that

$$\Delta P_{\mathrm{m,H}}(t) = \left(-\Delta\Gamma_{\mathrm{G}}e^{-\frac{t}{T_{\mathrm{G}}}} + \Gamma_{\mathrm{ss,G}}\right)\left(\frac{S_{\mathrm{b}}^{\mathrm{MG}}}{P_{\mathrm{b}}^{\mathrm{H}}}\right), \tag{10a}$$

$$\Delta P_{\mathrm{B}}^{*}(t) = \left(\Delta\Gamma_{\mathrm{fc}}e^{-\frac{t}{T_{\mathrm{fc}}}} + \Gamma_{\mathrm{ss,fc}}\right)\left(\frac{S_{\mathrm{b}}^{\mathrm{MG}}}{P_{\mathrm{b}}^{\mathrm{B}}}\right), \tag{10b}$$

where $\Delta\Gamma_{\mathrm{G}} = \Gamma_{\mathrm{ss,G}} - \Gamma_{\mathrm{tr,G}}$ and $\Delta\Gamma_{\mathrm{fc}} = \Gamma_{\mathrm{tr,fc}} - \Gamma_{\mathrm{ss,fc}}$. Since the hydro governor bandwidth is at a much lower frequency as compared to penstock and actuator dynamics (see Figure 4), the dynamics of the subsequent ones are neglected when obtaining Equation (10a). The total change in power is the summation of Equations (10a) and (10b), expressed with respect to microgrid base power, that is,

$$\Delta P_{\mathrm{tot}}(t) = \Delta\Gamma_{\mathrm{fc}}e^{-\frac{t}{T_{\mathrm{fc}}}} - \Delta\Gamma_{\mathrm{G}}e^{-\frac{t}{T_{\mathrm{G}}}} + \Gamma_{\mathrm{ss,tot}}, \tag{11}$$

where $\Gamma_{\mathrm{ss,tot}} = \Gamma_{\mathrm{ss,G}} + \Gamma_{\mathrm{ss,fc}}$. The first-order Taylor series expansion of Equation (11) gives

$$\begin{aligned}\Delta P_{\mathrm{tot}}(t) &\approx \Delta P_{\mathrm{tot}}(t=0) + \frac{d\Delta P_{\mathrm{tot}}(t)}{dt}\Big|_{t=0} t\\ &= \Delta\Gamma_{\mathrm{fc}}\left(1 - \frac{1}{T_{\mathrm{fc}}}t\right) - \Delta\Gamma_{\mathrm{G}}\left(1 - \frac{1}{T_{\mathrm{G}}}t\right) + \Gamma_{\mathrm{ss,tot}}.\end{aligned} \tag{12}$$

Applying the condition in Equations (9)–(12), the minimum time constant of the BESS frequency controller obtained is

$$T_{\mathrm{fc}} = \frac{\Delta\Gamma_{\mathrm{fc}}}{\Delta\Gamma_{\mathrm{G}}}T_{\mathrm{G}} = \frac{\Gamma_{\mathrm{tr,fc}} - \Gamma_{\mathrm{ss,fc}}}{\Gamma_{\mathrm{ss,G}} - \Gamma_{\mathrm{tr,G}}}T_{\mathrm{G}}. \tag{13}$$

By substituting Equations (2), (6) and (8) in Equation (13), the time constant becomes

$$T_{\mathrm{fc}} = \left[1 - R_{\mathrm{G}}\Delta P_{\mathrm{dm}}\left(\frac{1}{\Delta f^{\mathrm{max}}} - \frac{1}{\Delta f_{\mathrm{ss}}^{\mathrm{max}}}\right)\frac{S_{\mathrm{b}}^{\mathrm{MG}}}{P_{\mathrm{b}}^{\mathrm{H}}}\right]\frac{(1 + R_{\mathrm{G}}K_{\mathrm{p,G}})^{2}}{R_{\mathrm{G}}K_{\mathrm{i,G}}}. \tag{14}$$

Only the HPP provides steady-state power

This case arises when the HPP provides the total reserve in a steady state, whereas BESS provides no reserve in a steady state ($\Gamma_{\mathrm{ss,fc}} = 0$). Thus, the BESS frequency controller reduces to a high-pass filter (see Equation (3)). This case is applicable when the hydro turbine droop constant is given by $\frac{1}{R_{\mathrm{G}}} \geq \left(\left|\frac{\Delta P_{\mathrm{dm}}}{\Delta f_{\mathrm{ss}}^{\mathrm{max}}}\right| - D_{\mathrm{L}}\right)\left(\frac{S_{\mathrm{b}}^{\mathrm{MG}}}{P_{\mathrm{b}}^{\mathrm{H}}}\right)$ (see Section 3.2). By substituting Equations (2), (6) and (8) in Equation (13), the time constant becomes

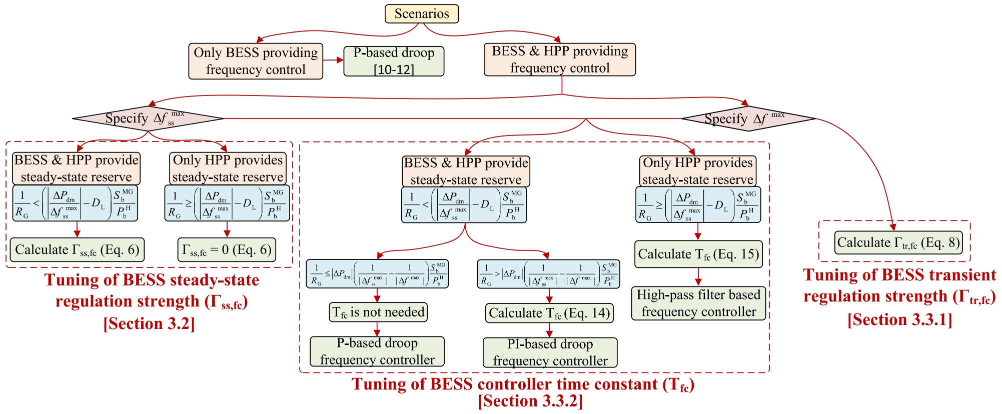

FIGURE 5 Flow chart of the proposed BESS frequency controller design and tuning.

$$T_{\mathrm{fc}} = -\frac{\Delta P_{\mathrm{dm}} + D_{\mathrm{L}}\Delta f^{\max}}{\Delta f^{\max}} \frac{\left(1 + R_{\mathrm{G}}K_{\mathrm{p,G}}\right)^2}{K_{\mathrm{i,G}}} \frac{S_{\mathrm{b}}^{\mathrm{MG}}}{P_{\mathrm{b}}^{\mathrm{H}}}. \tag{15}$$

Figure 5 summarises all the scenarios and the corresponding tuning of the BESS frequency controller proposed in this section.

4 | MICROGRID CASE STUDY AND FREQUENCY STABILITY ANALYSIS

4.1 | Description of hydro-powered industrial microgrid

The dimensioning disturbance for the smooth island transition of the microgrid depends on the maximum power import from the main grid (P_{G} in Figure 1). Figure 6 shows the time duration curve of the import power P_{G}, which is measured in 2018 at a substation in the west coast of Sweden. The measurement data has an hourly resolution. The negative value indicates power export to the main grid. The imported power is below 10.3 MWh/h for 98% of the year, which is considered to be the dimensioning disturbance ΔP_{dm} for the unplanned island transition of the microgrid [30]. Even though the maximum export power is also relatively high, it can be handled by automatically switching on the factory electric boiler once an over-frequency event is detected. Thus, only the power import scenario is considered for the dimensioning disturbance of the microgrid.

Table 1 [20, 31, 32], summarises the dimensioning disturbance, frequency performance criteria, load and hydro turbine-governor parameters (see Figure 2) for the dynamic frequency studies of the industrial microgrid. For a smooth island transition, the minimum allowed frequency nadir is set to 49 Hz, that is, $|\Delta f^{\max}| = 0.02$ p.u. (1 Hz) [32], whereas the maximum steady-state frequency deviation is $|\Delta f_{\mathrm{ss}}^{\max}| = 0.01$ p.u. (0.5 Hz). In this paper, the microgrid base power is chosen to be equal to the HPP rated active power, that is, $S_{\mathrm{b}}^{\mathrm{MG}} = P_{\mathrm{b}}^{\mathrm{H}} = 46.3$ MVA.

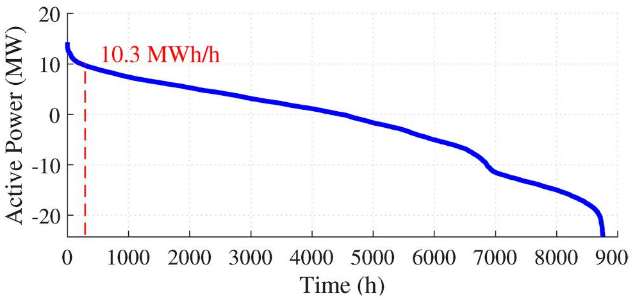

FIGURE 6 Time duration curve of the measured active power exchange between the upstream grid and the microgrid in 2018, where positive values indicate import to microgrid. The dimensioning disturbance of 10.3 MWh/h corresponds to 98 percentile of the curve.

4.2 | Parameter tuning of BESS frequency controller

Figure 7 (top) shows the resulting tuning of the steady-state gain $\Gamma_{\mathrm{ss,fc}}$, the transient gain $\Gamma_{\mathrm{tr,fc}}$ and the time constant T_{fc} of the proposed PI-based droop frequency controller for the BESS. The top figure is plotted according to Equations (6), (8), (14) and (15) as the hydro governor droop constant R_{G} increases from 1% to 10%. First, when the hydro governor droop increases from 1% to 4.5%, the hydro generator supplies the load fully in a steady state during island operation, and thus the steady-state gain of BESS $\Gamma_{\mathrm{ss,fc}} = 0$. The transient gain of the BESS $\Gamma_{\mathrm{tr,fc}}$ is constant and equal to 11.1 p.u., which is mainly determined by

TABLE 1 Microgrid dimensioning disturbance, frequency performance criteria [32], load and hydro turbine-governor parameters [20, 31].

Parameter	Value	Base	Parameter	Value	Base
Design parameters			Hydro turbine		
$\lvert\Delta f^{\max}\rvert$	0.02 p.u.	f_{b}	T_{y}	0.2 s	-
$\lvert\Delta f_{\mathrm{ss}}^{\max}\rvert$	0.01 p.u.	f_{b}	T_{w}	1.6 s	-
ΔP_{dm}	0.22 p.u.	$S_{\mathrm{b}}^{\mathrm{MG}}$	H_{H}	4.5 s	$S_{\mathrm{b}}^{\mathrm{H}}$
D_{L}	0 p.u.	$S_{\mathrm{b}}^{\mathrm{MG}}/f_{\mathrm{b}}$	Base values		
Hydro governor			f_{b}	50 Hz	-
R_{G}	0.05 p.u.	$f_{\mathrm{b}}/P_{\mathrm{b}}^{\mathrm{H}}$	$S_{\mathrm{b}}^{\mathrm{H}}$	54.5 MVA	-
$K_{\mathrm{p,G}}$	1.0 p.u.	$P_{\mathrm{b}}^{\mathrm{H}}/f_{\mathrm{b}}$	$P_{\mathrm{b}}^{\mathrm{H}}$	46.3 MW	-
$K_{\mathrm{i,G}}$	0.33 rad/s	$P_{\mathrm{b}}^{\mathrm{H}}/f_{\mathrm{b}}$	$S_{\mathrm{b}}^{\mathrm{MG}}$	46.3 MVA	-

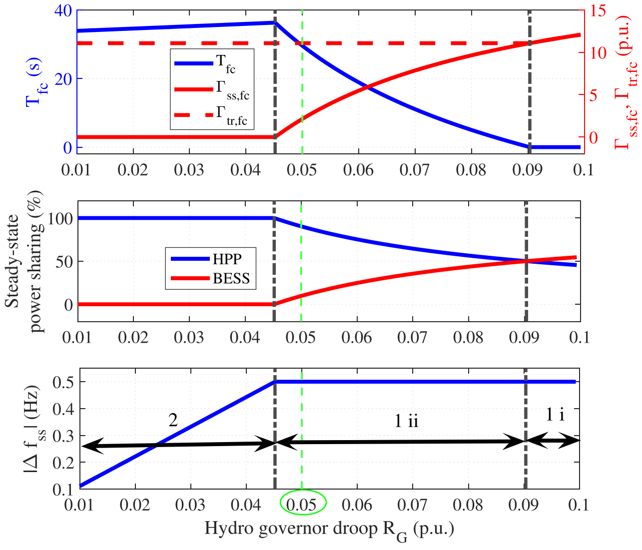

FIGURE 7 BESS frequency controller tuning (top), percentage of power sharing between HPP and BESS in steady state (middle) and steady-state frequency deviation (bottom) at different hydro governor droop constants. The three different regions, 1 i, 1 ii and 2, are illustrated in Figure 5. The green dashed line corresponds to the tuning selected for the dynamic analysis.

TABLE 2 BESS grid forming control parameters.

Parameter	Value	Base	Parameter	Value	Base
	Virtual impedance			Frequency controller	
R_{V}	0.075 p.u.	$Z_{\mathrm{b}}^{\mathrm{B}}$	$K_{\mathrm{p,fc}}$	49.3 p.u.	$P_{\mathrm{b}}^{\mathrm{B}}/f_{\mathrm{b}}$
L_{V}	0.15 p.u.	$L_{\mathrm{b}}^{\mathrm{B}}$	$K_{\mathrm{i,fc}}$	0.337 rad/s	$P_{\mathrm{b}}^{\mathrm{B}}/f_{\mathrm{b}}$
	Voltage controller		R_{fc}	0.1 p.u.	$f_{\mathrm{b}}/P_{\mathrm{b}}^{\mathrm{B}}$
Z_{T}	0.06 p.u.	$Z_{\mathrm{b}}^{\mathrm{B}}$		Base values	
$K_{\mathrm{i,vc}}$	52.36 rad/s	-	f_{b}	50 Hz	-
	Active power controller		ω_{b}	$2\pi(f_{\mathrm{b}})$ rad/s	-
$K_{\mathrm{p,pc}}$	0.011 p.u.	$f_{\mathrm{b}}/P_{\mathrm{b}}^{\mathrm{B}}$	V_{b}	400 V	-
$K_{\mathrm{i,pc}}$	0.35 rad/s	$f_{\mathrm{b}}/P_{\mathrm{b}}^{\mathrm{B}}$	$S_{\mathrm{b}}^{\mathrm{B}}$	11 MVA	-
K_{a}	0.022 p.u.	$f_{\mathrm{b}}/P_{\mathrm{b}}^{\mathrm{B}}$	$P_{\mathrm{b}}^{\mathrm{B}}$	10.5 MW	-
α_{pc}	62.8 rad/s	-	$Z_{\mathrm{b}}^{\mathrm{B}}$	0.0145 Ω	-
			$L_{\mathrm{b}}^{\mathrm{B}}$	46.3 μH	-

TABLE 3 Selected parameters for the BESS frequency controller and hydro governor. All values are in per unit with respect to microgrid base power, that is, $S_{\mathrm{b}}^{\mathrm{MG}} = P_{\mathrm{b}}^{\mathrm{H}} = 46.3$ MVA.

$\Gamma_{\mathrm{ss,fc}}$	2.2 p.u.	$\Gamma_{\mathrm{tr,fc}}$	11.1 p.u.	T_{fc}	29.4 s
$\Gamma_{\mathrm{ss,G}}$	20 p.u.	$\Gamma_{\mathrm{tr,G}}$	0.95 p.u.	T_{G}	63 s

the dimensioning disturbance and the frequency nadir requirement according to Equation (8). The time constant T_{fc} slightly increases as the hydro governor droop increases up to 4.5% according to Equation (15). Second, as the hydro governor droop increases from 4.5% to 9%, the BESS starts to provide more and more steady-state reserves with $\Gamma_{\mathrm{ss,fc}}$ increasing from 0 to 11.1 p.u. according to (6). The transient gain $\Gamma_{\mathrm{tr,fc}}$ remains unchanged, whereas the time constant T_{fc} starts to decrease as BESS increases its steady-state power sharing. Third, as the hydro governor droop constant increases above 9%, the BESS increases its steady-state power sharing such that the steady-state gain becomes higher than the minimum threshold for the transient gain. In this case, the transient gain of the BESS $\Gamma_{\mathrm{tr,fc}}$ is set equal to its steady-state gain $\Gamma_{\mathrm{ss,fc}}$, and the time constant is equal to zero. In the following dynamic analysis, a hydro governor droop constant of 5% is considered. The corresponding BESS frequency controller tuning is illustrated with the green dotted line in Figure 7. Table 2 shows the parameters for the BESS GFM control (see Figure 3), whereas Table 3 shows the selected tuning for the BESS frequency controller and hydro governor.

4.3 | Microgrid small-disturbance stability

To analyse how the proposed frequency controller of the BESS affects the small-disturbance stability of the microgrid during island operation, the response of the microgrid frequency Δf_{MG} is evaluated when subject to an imbalance in active power ΔP_{L}, that is, $\frac{\Delta f_{\mathrm{MG}}(s)}{\Delta P_{\mathrm{L}}(s)}$. The microgrid frequency is calculated following the concept of frequency of centre of inertia as described in Ref. [33]. The microgrid is linearised with the aid of a Simulink Model Lineariser. The initial operating point considered for linearisation is illustrated in Table 4 (inside parenthesis). In this study, the factory is modelled as a constant power load, which is the worst case scenario in terms of stability. Figure 8 (top) shows the zero-pole map of the closed-loop transfer function $\frac{\Delta f_{\mathrm{MG}}(s)}{\Delta P_{\mathrm{L}}(s)}$ when the BESS is not equipped with a frequency controller. The dominant complex poles have an oscillation frequency of 0.174 rad/s with a damping ratio of 0.1. The bottom plot shows the movement of these two complex poles when the BESS is equipped with the frequency controller while sweeping different values of the transient gain $\Gamma_{\mathrm{tr,fc}}$ and time constant T_{fc} of the controller. The steady-state gain $\Gamma_{\mathrm{ss,fc}}$ is set to zero in this analysis, but the impact of the steady-state gain on the small signal stability is illustrated later. When the transient gain is increased from 0 to 11.1 p.u. (blue color) or the time constant is increased from 0 to 29.4 s (red color), the damping ratio of the two complex poles increases from 0.1 to 0.7. This indicates that a BESS frequency controller with a larger transient gain and time constant improves the damping of the microgrid frequency in island operation. The sensitivity to the steady-state gain has also been tested by sweeping $\Gamma_{\mathrm{ss,fc}}$ from 0 to 2.2 p.u., which results in increasing the damping ratio of the complex poles further from 0.7 to 0.76 (result is not shown in the paper). It is worth mentioning that the aforementioned tests have also been done with different operating points of the BESS, that is, $P_{\mathrm{B},0}^{*} = 0$ MW and $P_{\mathrm{B},0}^{*} = 10$ MW. The results are very similar and therefore not shown in this paper. For the following dynamic simulation, the steady-state gain $\Gamma_{\mathrm{ss,fc}} = 2.2$ p.u., the transient gain $\Gamma_{\mathrm{tr,fc}} = 11.1$ p.u., and the time constant $T_{\mathrm{fc}} = 29.4$ s are used for the BESS frequency controller as listed in Table 3.

Using the same control parameters as in Table 3, the bode diagram of the open loop transfer function $\frac{\Delta f_{\mathrm{B}}}{\Delta f_{\mathrm{B}}^{*}}$ is shown in Figure 9. The loop is open by removing the feedback signal Δf_{B}

TABLE 4 Steady-state power flow of the microgrid in Figure 1 before (outside parenthesis) and after the disturbance (inside parenthesis). The post-disturbance power flow corresponds to the base case scenario in this paper.

	Active power (MW)	Reactive power (MVAr)	Voltage (p.u.)
Grid	$P_G = 10.3$ (0)	$Q_G = 10.5$ (0)	$V_{pcc} = 1$ (0.9815)
HPP	$P_H = 8.1$ (17.4)	$Q_H = 0.07$ (8.7)	$V_H = 1$ (1)
BESS	$P_B = 0$ (1)	$Q_B = 1.24$	$V_L = 0.993$ (0.979)
Factory	$P_L = 18.4$ (18.4)	$Q_L = 10.8$ (10.8)	$V_L = 0.993$ (0.979)

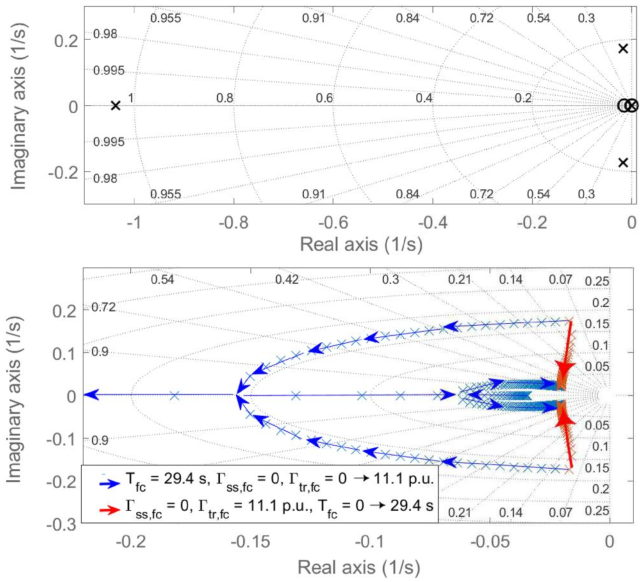

FIGURE 8 Zero-pole map of the closed loop transfer function between the factory active power demand and the frequency of centre of inertia of the microgrid in island operation when BESS frequency controller is disabled (top); corresponding root loci of the dominant pair of poles when changing BESS frequency controller parameters (bottom).

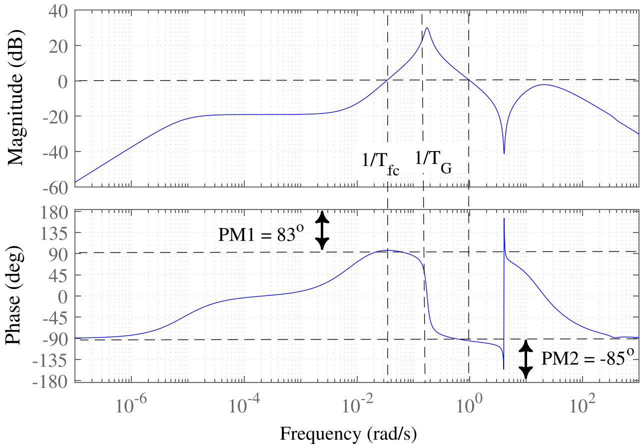

FIGURE 9 Bode magnitude and phase plots of BESS open frequency control loop $\frac{\Delta f_B}{\Delta f_B^*}$.

of the frequency controller. There are two crossover frequencies: 1) at 0.033 rad/s (0.0053 Hz) with a corresponding phase margin of 83° and 2) at 1 rad/s (0.159 Hz) with a corresponding phase margin of −85°. The system with the added BESS frequency controller is stable with relatively high phase margins between these two crossover frequencies. The dip in the bode magnitude plot at the frequency 4 rad/s (0.64 Hz) corresponds to the electro-mechanical oscillations between the BESS and the HPP.

5 | MICRODRID DYNAMIC SIMULATION RESULTS

The dynamic model of the microgrid shown in Figure 1 is implemented in Matlab/Simulink using phasor simulation. The factory load is simulated as a constant power load with no voltage or frequency dependency. As both the HPP and the factory are located very close to the substation, no medium voltage cables are modelled in the base case. The impact of the distance between the HPP and the factory will be discussed in Section 7. Table 4 shows the steady-state voltage and power flow before (outside parentheses) and after (inside parentheses) the islanding event of the microgrid according to the base case scenario. It can be seen from the power flow that the microgrid imports 10.3 MW and 10.5 MVAr from the main grid right before the islanding event. The default parameters of the HPP and BESS are summarised in Table 1, Table 2, and Table 3, if not otherwise stated.

5.1 | Comparison with existing coordinated frequency controllers between BESS and HPP

5.1.1 | PI-based droop versus P-based droop

Figure 10 shows the microgrid frequency (upper), active power output from the hydro generator P_H (middle) and the BESS P_B (bottom) during an islanding event, where the frequency controller of the BESS uses either the P-based or the PI-based droop control. The islanding event occurs at $t = 5$ s, before which the microgrid was importing 10.3 MW of active power from the main grid. For the P-based droop, two different settings of the proportional gain are shown, where one sets the proportional gain $K_{p,fc}$ to the desired steady-state regulation strength $\Gamma_{ss,fc} = 2.2$ p.u (low gain), and the other one sets $K_{p,fc}$ to the desired transient regulation strength $\Gamma_{tr,fc} = 11.1$ p.u. (high gain). The former tuning leads to a very low-frequency nadir of 46.6 Hz, while the latter one requires more active power and energy from the BESS in a steady state as shown in the bottom plot of the figure. As compared to the P-based droop, the PI-based droop has an additional degree of freedom, where the transient and steady-state gains can be set

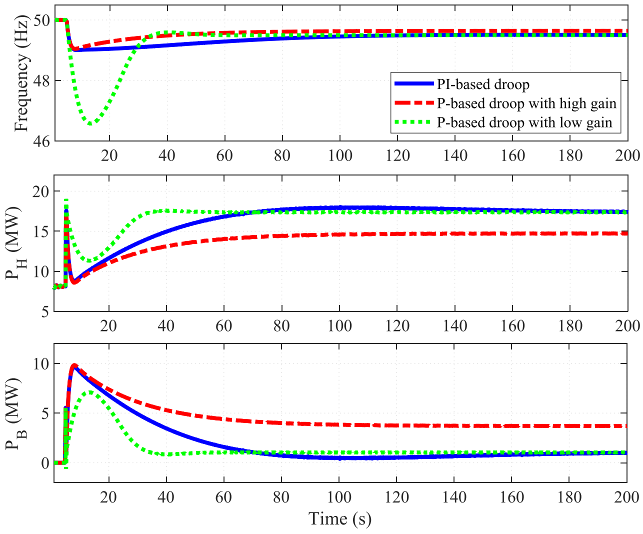

FIGURE 10 Impact analysis of the BESS frequency controller structure: frequency of centre of inertia (top), hydro generator active power P_{H} (middle), and BESS active power P_{B} (bottom).

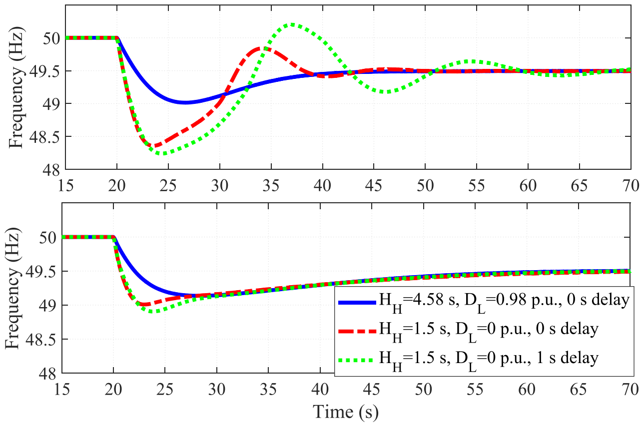

FIGURE 11 Frequency of centre of inertia when the microgrid is disconnected from the regional grid at t = 20 s while importing 0.07 p.u. (3.2 MW) of active power. The subplots correspond to the hydro governor and BESS frequency controller design according to Ref. [19] (top), or according to this paper (bottom). The sensitivity of the two strategies to the inertia constant of the HPP, load frequency dependence, and communication delay is displayed.

independently. Thus, the requirements for both the frequency nadir and the steady-state frequency can be fulfilled without unnecessarily consuming the energy storage. The secondary frequency control by the hydro turbine is not implemented here, which will bring the microgrid frequency back to 50 Hz and release the fast frequency reserve supplied by the BESS.

5.1.2 | Comparison with virtual power plant with 4th order frequency controller

In Ref. [19], a virtual power plant composed of a hydro turbine and a BESS is proposed to ride through frequency disturbances in the Nordic synchronous area. The derived frequency controller of the BESS is a 4th order controller, which is modelled here for comparison with our PI-based droop controller for microgrid applications. The tuning of the 4th order frequency controller in Ref. [19] is made specific to a grid condition through trial and error, with 0.07 p.u. of power disturbance, 0.98 p.u. of load frequency dependence, and an inertia constant of 4.58 s. Therefore, the same per-unit values are also used here in the microgrid comparison (refer to Table 1 for base values). Actuator and water time constants are kept the same as in Table 1. Three cases are evaluated for both controllers:

- Case 1: $H_{\mathrm{H}} = 4.58$ s, $D_{\mathrm{L}} = 0.98$ p.u., and 0 s controller time delay in the hydro turbine-governor system;
- Case 2: $H_{\mathrm{H}} = 1.5$ s, $D_{\mathrm{L}} = 0$ p.u., and 0 s controller time delay in the hydro turbine-governor system;
- Case 3: $H_{\mathrm{H}} = 1.5$ s, $D_{\mathrm{L}} = 0$ p.u., and 1 s controller time delay in the hydro turbine-governor system.

Figure 11 [19] shows the frequency response when disconnecting the grid at t = 20 s while importing 0.07 p.u. (3.2 MW), with the BESS frequency controller and hydro governor implemented and tuned according to Ref. [19] (top), or according to this paper (bottom). Both BESS frequency control strategies manage to limit the frequency nadir to 49 Hz in Case 1. In fact, the 4th order frequency controller drives the frequency to steady state faster than the PI-based droop controller, which indicates that the 4th order controller has a relatively faster integral action. However, in Case 2, where the inertia constant of the HPP is reduced from 4.58 to 1.5 s and the load frequency dependence from 0.98 p.u. to 0 p.u., the control strategy of [19] becomes ineffective in limiting the frequency nadir to 49 Hz. This is because the RoCoF is relatively higher in this case (−0.32 Hz/s), which causes the microgrid frequency to drop faster and the hydro turbine to reach its maximum ramp rate limit. As a result, frequency oscillations are observed. The frequency oscillations may be even amplified when the hydro turbine-governor system has a time delay of 1 s as shown in Case 3. On the other hand, by tuning the BESS frequency controller according to this paper, the frequency nadir barely drops below 49 Hz, and no oscillations are observed even under low-inertia conditions and with a 1 s delay. Moreover, the BESS frequency controller in this paper is of 1th order, which makes it easier to tune as compared to the 4th order controller in Ref. [19].

5.2 | Sensitivity analysis on the tuning of the proposed PI-based droop controller

5.2.1 | Impact of controller time constant

Figure 12 shows the impact of BESS frequency controller time constant tuning on the frequency response. The base value of the controller time constant is 29.4 s (see Table 3). With a shorter controller time constant of 5 s, BESS reduces its

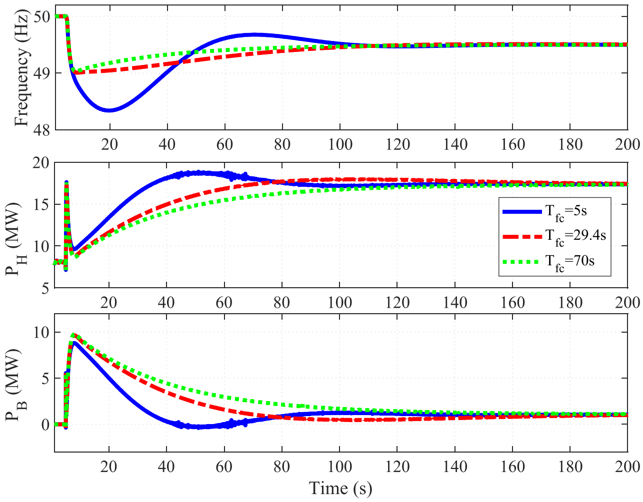

FIGURE 12 Impact analysis of the BESS frequency controller time constant: frequency of centre of inertia (top), hydro generator active power P_H (middle), and BESS active power P_B (bottom).

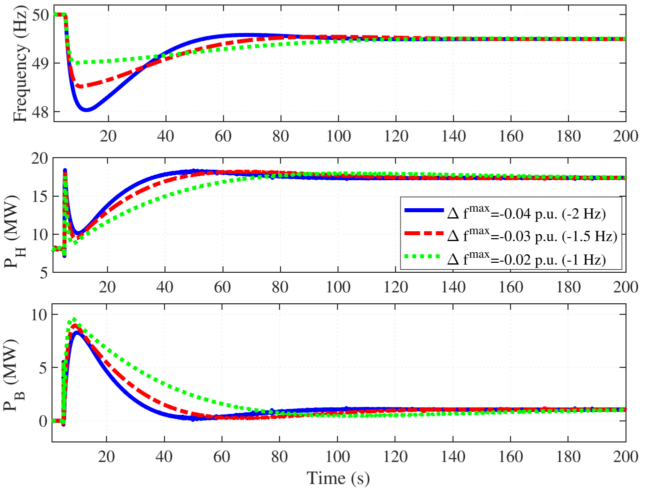

FIGURE 13 Impact analysis of maximum allowed frequency deviation: frequency of centre of inertia (top), hydro generator active power P_H (middle), and BESS active power P_B (bottom).

frequency reserve much quicker than the hydro turbine can increase its FCR. This leads to a poor frequency response with a frequency nadir of 48.34 Hz, which is below the requirement of 49 Hz. On the other hand, a longer controller time constant of 70 s will lead to a longer decay time of BESS frequency reserve, and thus, more energy consumption.

5.2.2 | Impact of performance criteria on frequency nadir

Figure 13 shows the corresponding results when the performance criteria of the minimum allowed frequency nadir is reduced from 49 to 48.5 Hz and to 48 Hz. As the minimum allowed frequency nadir is reduced from 49 to 48.5 Hz, the hydro turbine increases its FCR more quickly due to a larger frequency error signal. This shortens the frequency support duration of the BESS, allowing it to ramp down its power faster. Thus, less energy is required from the BESS. However, by further reducing the minimum allowed frequency nadir to 48 Hz, the reduced energy requirement of the BESS is no longer as significant. This is because the hydro turbine has reached its maximum ramp rate limit. Moreover, the maximum active power of the BESS is reduced slightly when relaxing the frequency nadir requirements. This is because of the longer time to reach the frequency nadir, which allows more time for the hydro turbine to increase its FCR.

6 | EXPERIMENTAL VALIDATION

6.1 | Laboratory setup

The proposed PI-based droop frequency controller and its tuning for the BESS is tested using a kW scale 400 V laboratory setup. Figure 14 shows the network diagram of the lab setup including ratings of each component, whereas Figure 15 shows a photo of the lab setup. The BESS is emulated using a 4-quadrant 30 kVA Regatron ACS power amplifier, which is essentially a controllable voltage source representing the behaviour of a VSI in the BESS. The controller of the BESS described in Figure 3 is implemented in dSPACE MicroLabBox that sends three-phase reference voltage signals to the amplifier. The amplifier is connected in parallel with the industrial load represented by a 30 kW induction motor. Tap-changing transformer is unavailable in the lab. Instead, switchable shunt capacitor banks are used to regulate the terminal voltage of the induction motor to be around 1 p.u. before the islanding event. The transformer impedance of the industry and the filter impedance of the BESS are both represented by a series inductor with an impedance of 0.05 + j0.95 Ω. The hydro generator is represented by a 75 kVA synchronous machine driven by a dc motor (turbine) including a flywheel to replicate the inertia of a hydro turbine. The hydro turbine-governor model described in Figure 2 and the generator excitation control are implemented in dSPACE 1103. The entire microgrid setup is connected to the local 400 V distribution grid.

6.2 | Experimental results and analyses

Three tuning strategies of the BESS frequency controller are tested:

1. Proposed PI-based droop ($\Gamma_{ss,fc} = 2.2$ p.u., $\Gamma_{tr,fc} = 11.1$ p.u., and $T_{fc} = 29.4$ s)
2. P-based droop with high gain ($\Gamma_{ss,fc} = \Gamma_{tr,fc} = 11.1$ p.u.)
3. P-based droop with low gain ($\Gamma_{ss,fc} = \Gamma_{tr,fc} = 2.2$ p.u.)

The pre-disturbance power flow of the three cases resembles each other and is summarised in Table 5. Figure 16 shows the microgrid frequency response, the PCC voltage angle, and active power output from the synchronous generator and the VSI

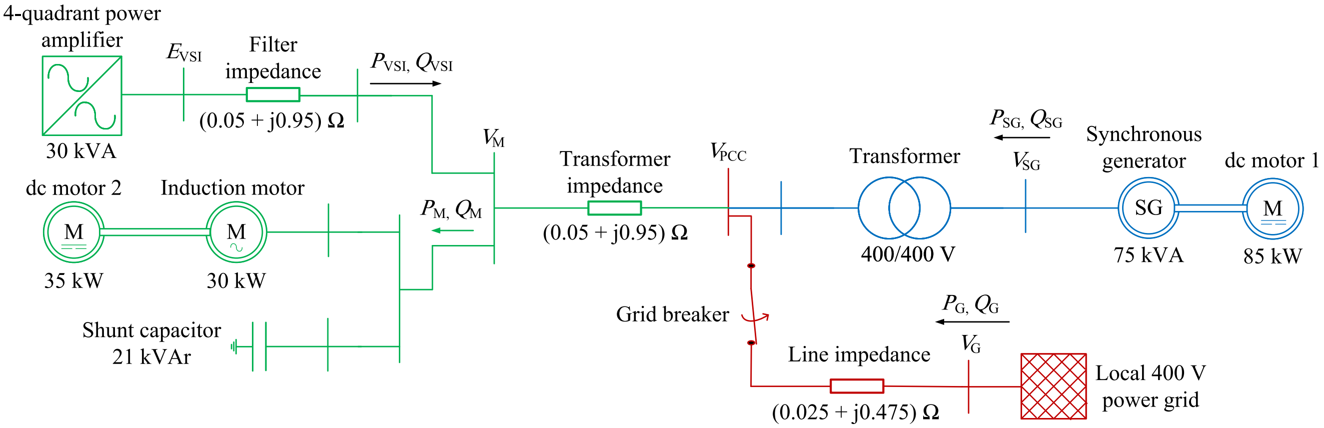

FIGURE 14 Network diagram of a laboratory setup: Paper and pulp factory replica (green), hydro turbine replica (blue), and local power grid (red).

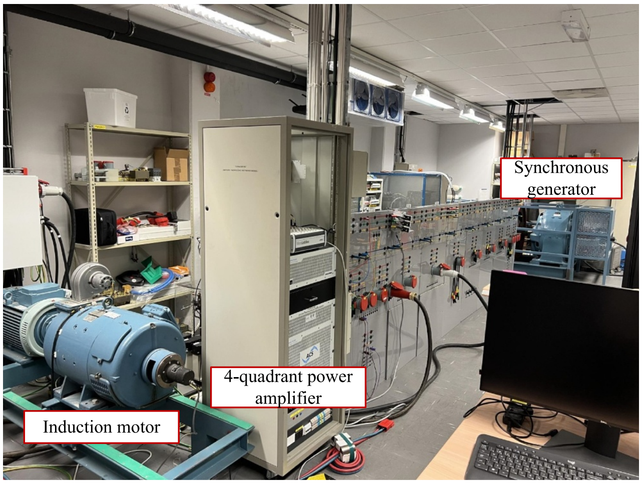

FIGURE 15 Photo of a laboratory setup.

TABLE 5 Pre-disturbance power flow of a laboratory test (see Figure 14).

	Active power	Reactive power
Grid	P_G = 14.4 kW	Q_G = 1 kVAr
Synchronous generator	P_{SG} = 4 kW	Q_{SG} = −1.2 kVAr
Power amplifier	P_{VSI} = 0 kW	Q_{VSI} = 0 kVAr
Induction motor & shunt capacitor	P_M = 18.2 kW	Q_M = −1.9 kVAr

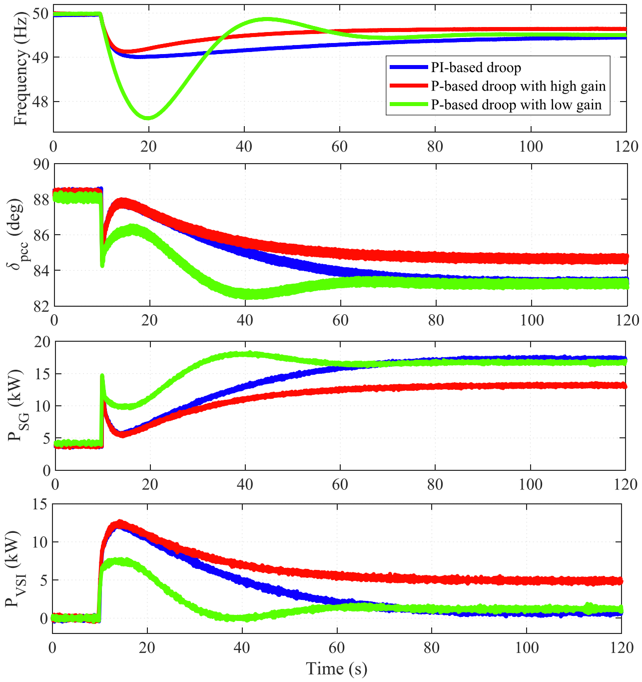

FIGURE 16 Laboratory test comparing the performance of P-based droop and PI-based droop when the grid breaker is opened at $t = 10$ s: synchronous generator frequency (top), PCC voltage angle with respect to the rotor flux of the synchronous generator (top middle), synchronous generator active power (bottom middle) and voltage source inverter active power (bottom).

(power amplifier) when an unintentional islanding occurs. Right before the islanding event, the microgrid imports 14.4 kW and 1 kVAr from the local grid. In all the three cases, once the grid is disconnected, an angle jump of around 4° is experienced at the PCC as shown in the top middle plot (the angle is measured with respect to the rotor flux of the synchronous generator). Since both the synchronous generator and the GFM VSI have a stiff back emf angle, they will both experience a sudden increase in the active power at their terminal, as shown in the bottom middle and bottom plots, respectively. As the synchronous generator is electrically closer to the disturbance, it experiences a larger active power disturbance at its terminal as compared to the VSI. However, due to the fast frequency response of the VSI, the active power output from the VSI ramps up quickly to limit the frequency drop within the microgrid whereas the turbine-governor system of the synchronous generator slowly ramps up its mechanical power. In the case where the BESS frequency controller uses the P-based droop with low gain, the frequency nadir went down to 47.6 Hz, where the protection would shut down the whole microgrid in reality. The frequency nadir is limited to 49.1 Hz if the proportional gain of the P-based droop is increased from 2.2 p.u. to 11.1 p.u. However, this results in a relatively high energy storage demand from the VSI as shown in the bottom middle plot of the figure. This may become an issue

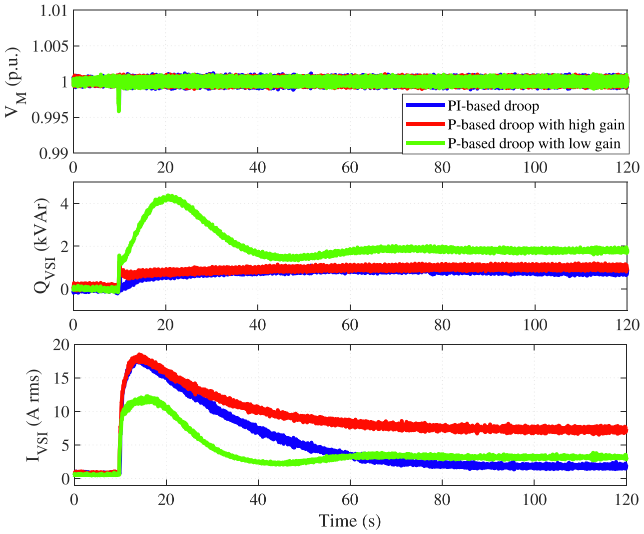

FIGURE 17 Laboratory test comparing the performance of P-based droop and PI-based droop when the grid breaker is opened at $t = 10$ s: induction motor terminal voltage (top), voltage source inverter reactive power (middle), and voltage source inverter rms current (bottom).

in reality when the storage capacity is very limited and easily depleted. On the other hand, the proposed PI-based droop is able to fulfill the requirement for the frequency nadir while using as low energy storage as possible. This is achieved by tuning the steady-state gain of the BESS frequency controller to be relatively smaller than the transient gain, with a time constant tuned considering the regulating speed of the hydro turbine-governor system as described in Section 3.3.2. Both the transient gain and the time constant play an important role in limiting the frequency nadir to a desired value.

Figure 17 (top) shows the VSI terminal voltage (V_M in Figure 14) during the island transition. In all three cases, the voltage dips to 0.996 p.u. right after the disturbance. This causes the VSI reactive power to rise immediately since it is controlled in the GFM control model. The voltage controller then takes action and regulates the terminal voltage to 1 p.u. In the case of PI-based droop and P-based droop with high gain, the reactive power needed by the VSI is very little, 0.7 kVAr and 1.1 kVAr, respectively, as shown in the middle subplot. This is because both the VSI and the synchronous generator are supplying the induction motor through a relatively small impedance with a high X/R ratio, that is, $0.05 + j0.95\ \Omega$ ($0.0094 + j0.18$ p.u. under 30 kVA and 400 V base). In the case of a P-based droop with low gain, the reactive power needed is much larger (4.3 kVAr). This is because of the low-frequency nadir in this case (see Figure 16 top), which leads to a reduction in the back EMF of the induction motor and thus larger reactive power demand. In both cases where the frequency nadir is fulfilled, the PI-based droop control has a similar maximum current as the P-based droop control. In other words, the current rating of the VSI is not increased with the proposed PI-based droop as compared to the traditional P-based droop.

7 | FURTHER DISCUSSION

The maximum RoCoF is not considered as a dimensioning criterion in this paper. However, in a microgrid with very low synchronous inertia, synthetic inertia can be provided by the BESS to limit the RoCoF in case of a large power imbalance. The synthetic inertia can be implemented by adjusting the bandwidth of the active power control loop of the BESS [27] or added as an outer loop together with the frequency controller [34].

If the grid-tie breaker (breaker CB in Figure 1) signal of the microgrid should be lost, local measurement signals such as frequency can be used as a backup for island detection. One common passive island detection method is to use frequency deviation as a criterion [29]. If the threshold for the frequency-based island detection method is set to 49 Hz, then the frequency nadir may drop slightly below 49 Hz before the BESS can ramp up its power to bring the frequency back to its acceptable limit.

There is no significant power oscillations observed in the cases analysed, even when the distance between the HPP and BESS is increased to 30 km. One reason is that the power rating of the BESS is about 5 times smaller than the hydro generator. Another reason is that the BESS is typically designed to provide a large damping power [35, 36]. However, power oscillation may start to appear if the two power sources of comparable sizes are connected through a long cable and that the BESS provides little or no damping as illustrated in Ref. [37]. Such a power oscillation can be attenuated with a proper tuning of the active power controller of the BESS.

8 | CONCLUSIONS

This paper has developed a simple yet effective frequency control strategy for the BESS to facilitate a smooth island transition of a hydro-powered microgrid. The proposed frequency controller uses a PI-based droop, whereas the tuning strategy of the controller accounts for the limitations in the power response of a hydro generator and the desired frequency performance criteria set by the microgrid operator, without over-dimensioning the size of the storage capacity. The effectiveness of the proposed frequency control strategy is demonstrated both in simulation and laboratory tests. The storage capacity requirement of the BESS depends mainly on the steady-state droop and regulating speed of the hydro turbine-governor system, whereas the power capacity depends mainly on the dimensioning disturbance of the microgrid, that is, the maximum import/export power of the microgrid in this case. The storage capacity may be further reduced if the frequency nadir requirement is relaxed, provided the maximum ramp rate limit of the hydro turbine is not reached.

AUTHOR CONTRIBUTIONS

Ahmed Sunjaq: Conceptualisation; Data curation; Investigation; Methodology; Software; Validation; Visualisation; Writing – original draft. **Peiyuan Chen**: Conceptualisation; Investigation; Supervision; Validation; Writing – original draft; Writing – review & editing. **Massimo Bongiorno**: Supervision; Writing – review & editing. **Ritwik Majumder**: Supervision; Writing – review & editing. **Jan Svensson**: Supervision; Writing – review & editing

ACKNOWLEDGEMENT

European Union's Horizon 2020 research and innovation programme. Grant/award number: 646039 and 775970.

CONFLICT OF INTEREST STATEMENT

The authors certify that they have no affiliations with or involvement in any organisation or entity with any financial interest (such as honoraria, educational grants, participation in speakers' bureaus, membership, employment, consultancies, stock ownership, or other equity interest and expert testimony or patent-licensing arrangements) or non-financial interest (such as personal or professional relationships, affiliations, knowledge, or beliefs) in the subject matter or materials discussed in this manuscript.

DATA AVAILABILITY STATEMENT

The data that support the findings of this study are available from Vattenfall Eldistribution AB. Restrictions apply to the availability of these data, which were used under license for this study. Data are available from the authors with the permission of Vattenfall Eldistribution AB.

ORCID

Ahmed Sunjaq https://orcid.org/0000-0002-3380-6778

REFERENCES

1. World Business Council for Sustainable Development (WBCSD). Microgrids for Commercial and Industrial Companies. [Internet]. WBCSD, Geneva (2017). [cited 2023 May 10] https://docs.wbcsd.org/2017/11/WBCSD_microgrid_INTERACTIVE.pdf
2. Hitachi ABB Power Grids: Reliable, Affordable Power with Substantial Energy Savings at an Industrial Facility. Hitachi ABB Power Grids, Zurich (2021). [cited 2023 May 10] https://library.e.abb.com/public/e7bfff1820de4f4a82eab43afc2db764/Commercial-case-study-9AKK107045A3118-A4.pdf?x-sign=lkbhnYKxiIcIlFdwFByypMK4aGzd6rujBb1SQXvzcaVfW/LCZoecxJ2esgc5UcvK
3. Hitachi ABB Power Grids: Ensuring Reliable Power for Commercial and Industrial Site. Hitachi ABB Power Grids, Zurich (2021). [cited 2023 May 11] https://search.abb.com/library/Download.aspx?DocumentID=4CAE000425\&LanguageCode=en\&Action=Launch
4. Vattenfall: Lilla Edet. [cited 2023 May 11] https://fiskevatten.vattenfall.com/lilla-edet/
5. High Voltage Valley: Ödrift - ett lager med fossilfri energi. [cited 2023 May 11] https://www.highvoltagevalley.se/sv-SE/projekt/?-?-?C3?-?-?B6drift-i-krafttanken-41360184
6. Platero, C., et al.: Hydropower plants frequency regulation depending on upper reservoir water level. Energies 12(9), 1637–1651 (2019). https://doi.org/10.3390/en12091637
7. Martínez-Lucas, G., et al.: Power-frequency control of hydropower plants with long penstocks in isolated systems with wind generation. Renew. Energy 83, 245–255 (2025). https://doi.org/10.1016/j.renene.2015.04.032
8. Yang, W., et al.: Frequency stability of isolated hydropower plant with surge tank under different turbine control modes. Elec. Power Compon. Syst. 43(15), 1707–1716 (2015). https://doi.org/10.1080/15325008.2015.1049722
9. Ung, N.: The Effects of Backlash on the Frequency Stability in a Hydro Based Power System [master's thesis on the Internet]. KTH University, Stockholm (2018). [cited 2023 May 10] https://www.svk.se/siteassets/5.jobba-har/dokument-exjobb/the-effects-backlash-on-frequency-stability-in-hydro-based-power-system.pdf
10. Hatziargyriou, N., et al.: Microgrids. IEEE Power Energy Mag. 5(4), 78–94 (2007). https://doi.org/10.1109/MPAE.2007.376583
11. Karimi-Ghartemani, M., et al.: Universal controller for three-phase inverters in a microgrid. IEEE J. Emerg. Sel. Top. Power Electron. 4(4), 1342–1353 (2016). https://doi.org/10.1109/JESTPE.2016.2614956
12. Ashabani, S., Mohamed, Y.: A flexible control strategy for grid-connected and islanded microgrids with enhanced stability using nonlinear microgrid stabilizer. IEEE Trans. Smart Grid 3(3), 1291–1301 (2012). https://doi.org/10.1109/TSG.2012.2202131
13. Gao, F., Iravani, M.: A control strategy for a distributed generation unit in grid-connected and autonomous modes of operation. IEEE Trans. Power Deliv. 23(2), 850–859 (2008). https://doi.org/10.1109/TPWRD.2007.915950
14. Pilehvar, M., Mirafzal, B.: Frequency and voltage supports by battery-fed smart inverters in mixed-inertia microgrids. Electronics 9(11), 1755–1768 (2020). https://doi.org/10.3390/electronics9111755
15. Kenyon, R., et al.: Using a grid-forming inverter to stabilize a low-inertia power system – Maui Hawaiian island. In: ISGT-Europe, pp. 1–6. Novi (2022). https://doi.org/10.1109/ISGT-Europe54678.2022.9960290
16. Acharya, S., Moursi, M., Al-Hinai, A.: Coordinated frequency control strategy for an islanded microgrid with demand side management capability. IEEE Trans. Energy Convers. 33(2), 639–651 (2018). https://doi.org/10.1109/TEC.2017.2763186
17. Mondal, A., Illindala, M.: Improved frequency regulation in an islanded mixed source microgrid through coordinated operation of DERs and smart loads. IEEE Trans. Ind. Appl. 54(1), 112–120 (2018). https://doi.org/10.1109/TIA.2017.2761825
18. Narula, A., et al.: Coordinated control of grid-forming converters and hydro generators to enhance frequency quality of future power system. Elec. Power Syst. Res. 212, 212 (2022). https://doi.org/10.1016/j.epsr.2022.108456
19. Björk, J., Johansson, K., Dörfler, F.: Dynamic virtual power plant design for fast frequency reserves: coordinating hydro and wind. IEEE Tran. Control Network Syst. 10(3), 1266–1278 (2022). https://doi.org/10.1109/TCNS.2022.3181553
20. ENTSO-E: FCR-N Design of Requirements. ENTSO-E, Brussels (2017). [cited 2023 May 11] https://www.svk.se/contentassets/e5a38b7a16a443b290f5d49d42ea03c0/3---fcr-n-design-of-requirements.pdf
21. Cutsem, T., et al.: Test systems for voltage stability studies. IEEE Trans. Power Syst. 35(5), 4078–4087 (2020). https://doi.org/10.1109/TPWRS.2020.2976834
22. Wen, B., et al.: Analysis of D-Q small-signal impedance of grid-tied inverters. IEEE Trans. Power Electron. 31(1), 675–687 (2016). https://doi.org/10.1109/TPEL.2015.2398192
23. Rosso, R., et al.: Grid-forming converters: control approaches, grid-synchronization, and future trends—a review. IEEE Open J. Ind. Appl. 2, 93–109 (2021). https://doi.org/10.1109/OJIA.2021.3074028
24. Inamdar, S.: Passive Island Detection of Microgrid by Grid Forming Inverter [licentiate thesis on the Internet]. Chalmers University of Technology, Gothenburg (2022). [Cited 2023 May 10] https://research.chalmers.se/publication/532971/file/532971_Fulltext.pdf
25. Rodriguez, P., et al.: Control of grid-connected power converters based on a virtual admittance control loop. In: 2013 15th European Conference on Power Electronics and Applications (EPE), pp. 1–10. Lille, France (2013). https://doi.org/10.1109/EPE.2013.6634621

26. Harnefors, L., Zhang, L., Bongiorno, M.: Frequency-domain passivity-based current controller design. IET Power Electron. 1(4), 455–465 (2008). https://doi.org/10.1049/iet-pel:20070286
27. Narula, A., et al.: Tuning and evaluation of grid-forming converters for grid-support. In: 2021 23rd European Conference on Power Electronics and Applications (EPE'21 ECCE Europe), pp. 1–10. Ghent, Belgium (2021). https://doi.org/10.23919/EPE21ECCEEurope50061.2021.9570679
28. Vukojevic, A., Lukic, S.: Microgrid protection and control schemes for seamless transition to island and grid synchronization. IEEE Trans. Smart Grid 11(4), 2845–2855 (2020). https://doi.org/10.1109/TSG.2020.2975850
29. Samuelsson, O., Strath, N.: Islanding detection and connection requirements. In: 2007 IEEE Power Engineering Society General Meeting, pp. 1–6. Tampa, FL, USA (2007). https://doi.org/10.1109/PES.2007.385997
30. DOE: The Advanced microgrid. Integration and interoperability. DOE, USA (2014). [cited 2023 May 11] https://www.osti.gov/biblio/1204100
31. Näsström, J.: State-of-the-art Development Platform for Hydropower turbine Governors [master's thesis on the Internet]. Umeå: Umeå University (2017). [cited 2023 May 10] https://www.diva-portal.org/smash/get/diva2:1173833/FULLTEXT01.pdf
32. IVA Royal Swedish Academy of Engineering Sciences: Reliability in Sweden's electricity System. IVA Royal Swedish Academy of Engineering Sciences, Stockholm (2017). [cited 2023 May 11] https://www.iva.se/globalassets/info-trycksaker/vagval-el/201705-iva-vagvalel-leveranssakerhet-english-c.pdf
33. ENTSO-E.: Future System inertia. ENTSO-E, Brussels (2018). [cited 2023 May 11] https://eepublicdownloads.entsoe.eu/clean-documents/Publications/SOC/Nordic/Nordic_report_Future_System_Inertia.pdf
34. Imgart, P., et al.: A cascaded power controller for robust frequency ride-through of grid-forming converters. In: 2022 IEEE Energy Conversion Congress and Exposition (ECCE), pp. 1–8. Detroit (2022). https://doi.org/10.1109/ECCE50734.2022.9947721
35. Harnefors, L., et al.: Generic PLL-based grid-forming control. IEEE Trans. Power Electron. 37(2), 1201–1204 (2022). https://doi.org/10.1109/TPEL.2021.3106045
36. Harnefors, L., et al.: Robust analytic design of power-synchronization control. IEEE Trans. Ind. Electron. 66(8), 5810–5819 (2019). https://doi.org/10.1109/TIE.2018.2874584
37. Ganjian-Aboukheili, M., et al.: Seamless transition of microgrids operation from grid-connected to islanded mode. IEEE Trans. Smart Grid 11(3), 2106–2114 (2020). https://doi.org/10.1109/TSG.2019.2947651

How to cite this article: Sunjaq, A., et al.: Frequency control by BESS for smooth Island transition of a hydro-powered microgrid. IET Smart Grid. 1–15 (2023). https://doi.org/10.1049/stg2.12140